Contribution to the electron distribution analysis. I. Shell structure of atoms

Miroslav Kohout, Andreas Savin, and Heinzwerner Preuss
Institut für Theoretische Chemie, Universität Stuttgart, Pfaffenwaldring 55, 7000 Stuttgart 80, Germany

(Received 13 February 1991; accepted 23 April 1991)

Relativistic spherically averaged numerical all-electron densities ρ were computed for the atoms Be–Ba, B–Tl, C–Pb, Cu–Au, and Zn–Hg. The Laplacian of these densities is not able to resolve the valence shell from the inner shells in case of heavy atoms, starting with the fourth row. The distribution of the local kinetic energy $E_{\rm kin}$ shows a valence maximum even for these heavy atoms, unfortunately, in a region of negative kinetic energy; i.e., nonclassically allowed. The quantity $-|\nabla\rho|/\rho$ was also investigated. For all computed atoms, the $-|\nabla\rho|/\rho$ diagrams are capable of describing the complete shell structure. $-|\nabla\rho|/\rho$ is sensitive to basis set quality: poor Gaussian basis sets exhibit spurious oscillations and a premature onset of the linear decay. For the atoms B–Tl, Ba, Au, Hg, and Pb, nonrelativistic numerical calculations were performed to examine the effect of the relativity on the aforementioned quantities. Tests with pseudopotential densities reveal that for pseudopotential calculations, it is advisable to use at least two outermost shells in order to reproduce the all-electron values of $\nabla^2\rho$, $E_{\rm kin}$, and $-|\nabla\rho|/\rho$ in the valence region.

I. INTRODUCTION

Over the past few years there was a great interest in describing the shell structure of the electron density distribution of the atoms.[1-10] Hereinafter, shell stands for all the orbital density distributions with the same principal quantum number. The averaged electron density $\rho(r)$ of an atom in the ground state depicts a picture of high simplicity.[1] It is given by a peak at the atom position and a monotonic decay toward zero with increasing distance from the nucleus. Hence, the electron density itself is not appropriate for describing the shell structure.

The radial density distribution $D(r)=4\pi r^2\rho$ demonstrates more structure.[1-3] It displays several peaks, the number of which depends on the highest principal number of the investigated atom. The main contribution to a particular peak is given from the orbitals with the same principal quantum number. The largest (outermost) maxima of the radial distributions are located at close proximity for orbitals with the same principal quantum number. Thus, $D(r)$ should be able to reveal the shell structure. Unfortunately, this is true only for the light atoms. The higher the principal quantum number of a shell, the less perceptible is the corresponding peak. Consequently, in case of heavy atoms the valence shell is no more distinguishable.[1-3]

The Laplacian of the electron density indicates regions where charge is localy concentrated or depleted, whereby a positive value of $-\nabla^2\rho$ stands for charge concentration. In an atom, $-\nabla^2\rho$ exhibits spherical nodes which divide the space around the nucleus in regions with alternate positive and negative values of $-\nabla^2\rho$. Pairs of regions, one positive and one negative, represents the shell structure of the atom.[4,5] For each shell, one pair is expected. This is true for the light atoms. However, for some heavy atoms, starting with the fourth row, the Laplacian is not able to resolve the outermost shell from the core.[6,7] This will be further illustrated in the next section.

In the framework of the theory of the marginal and conditional amplitude function,[11,12] the electronic wave function $\Psi(\mathbf{r}s\,\mathbf{r}'s'|\mathbf{R})$, satisfying the Schrödinger equation, is factorized as

$$\Psi(\mathbf{r}s\,\mathbf{r}'s'|\mathbf{R})=\vartheta(\mathbf{r}|\mathbf{R})\chi(\mathbf{r}'s's|\mathbf{R}), \tag{1}$$

where $\mathbf{R}$ stands for the coordinates of the nuclei and $\mathbf{r}$ and s for the space and spin coordinates of a particular electron. The space and spin coordinates of the remaining electron are denoted by $\mathbf{r}'$ and s'. In the case of molecules, the functions are parametrically depending on $\mathbf{R}$. Here ϑ is the marginal amplitude function. Suppose ϑ and χ are normalized. ϑ is the electronic one-electron wave function linked to the theoretical electron density by

$$\rho(\mathbf{r}|\mathbf{R})=N|\vartheta(\mathbf{r}|\mathbf{R})|^2, \tag{2}$$

with N as the number of the electrons.

With Eqs. (1) and (2), the Schrödinger equation in the Born–Oppenheimer approximation was transformed by Hunter[8,13] into the following form:

$$-\hbar^2\{\nabla^2\rho(\mathbf{r}|\mathbf{R})/4-[\nabla\rho(\mathbf{r}|\mathbf{R})]^2/[8\rho(\mathbf{r}|\mathbf{R})]\}+U(\mathbf{r}\mathbf{R})\rho(\mathbf{r}|\mathbf{R})=E(\mathbf{R})\rho(\mathbf{r}|\mathbf{R}), \tag{3}$$

where $U(\mathbf{r}\mathbf{R})$ is an effective potential.

The Schrödinger equation for the electron density provides a model for the shell structure of the atomic charge distribution similar to the Laplacian. Equation (3) can be written as

$$U(\mathbf{r}\mathbf{R})-E(\mathbf{R})=\hbar^2\{\nabla^2\rho(\mathbf{r}|\mathbf{R})/[4\rho(\mathbf{r}|\mathbf{R})]-[\nabla\rho(\mathbf{r}|\mathbf{R})]^2/[8\rho(\mathbf{r}|\mathbf{R})^2]\}. \tag{4a}$$

The potential which appears on the left side of this equation can be regarded as the electron's negative local kinetic energy $-E_{\rm kin}$

$$-E_{\rm kin}=U-E. \tag{4b}$$

 0021-9606/91/151928-15$03.00

We did use Eq. (4a) with our relativistic densities (the sum of the densities for the small and the large component), though the derivation[13] was performed for the nonrelativistic case. In atoms, there are spherical regions of positive and negative kinetic energy $-E_{\rm kin}$. For each shell, a region of negative $-E_{\rm kin}$ is expected, where an electron is classically allowed.[8] The shells are separated by potential barriers of positive $-E_{\rm kin}$. But this statement holds only for light elements.[9] In the case of heavy elements, starting with Ga, there is a valence minimum in $-E_{\rm kin}$, but in a region of negative kinetic energy, the analysis of $-E_{\rm kin}$ is subject to the Sec. III.

For $r\to\infty$, the electron density of an atom is described by[14,15]

$$\sqrt{\rho(r)}\to r^{\varkappa}e^{-\lambda r}\quad \lambda=\sqrt{(-2{\rm IP})},$$
$$\varkappa=(Z-N+1)/\lambda-1. \tag{5}$$

IP is the ionization potential, Z the nuclear charge, and N the number of electrons. Let us suppose that $\varkappa=0$, then $-|\nabla\rho|/\rho$ is given by

$$-|\nabla\rho|/\rho=-2\lambda. \tag{6}$$

If the electron density of an atom is described by Eq. (5) with different λ for each shell,[16] then the shell structure is represented by a step-like $-|\nabla\rho|/\rho$ diagram. Every step in such a diagram can be associated with a particular shell. In the literature,[10,16] $\log(\rho)$ was used to reproduce the shell structure of atoms. The quantity $-|\nabla\rho|/\rho$ can be regarded as the slope of such $\log(\rho)$ vs r curves.[10] Section IV will be concerned with more details about $-|\nabla\rho|/\rho$.

In the case of the numerical calculations, the quantities $\nabla\rho$ and $\nabla^2\rho$ used to compute $-E_{\rm kin}$ [Eq. (4a)], $-|\nabla\rho|/\rho$, and $-\nabla^2\rho$ were numerically derived from the density values on a radial logarithmic grid. For $\nabla\rho$, we have utilized six, and in the case of $\nabla^2\rho$, nine points.

II. SHELL STRUCTURE WITH $-\nabla^2\rho$

For the IIa, IIIa, IVa, Ib, and IIb group atoms Be–Ba, B–Tl, C–Pb, Cu–Au, and Zn–Hg, respectively, the relativistic spherically averaged numerical all-electron densities were computed using the multiconfiguration Dirac–Fock (MCDF) program.[17] The Laplacian was numerically derived as described above. The number and the sign of the maxima and minima in $-\nabla^2\rho$ was examined. At the nucleus $-\nabla^2\rho$ is positive infinite.[6] This extremum will be denoted as the first maximum. The atoms of the second and third row are characterized by two (three) positive maxima and two (three) negative minima. This is indicative of the expected two (three) shells.[4]

Starting with the fourth row, the Laplacian is not able to resolve the valence shell from the core. Table I demonstrates that, in the valence region, the pair representing a shell—one positive maximum and a negative minimum, respectively—is missing. Thus, for the fourth row atoms Cu–Ge, we can locate merely three such pairs. Only four pairs are distin-

TABLE I. $-\nabla^2\rho$ maxima for the valence and the penultimate shell. The density was derived from a relativistic Dirac–Fock calculation (Ref. 17). All data are in atomic units. [n the principal quantum number of the valence shell; $(-\nabla^2\rho)_n$ nth $-\nabla^2\rho$ maximum; r_n^L the distance of the nth $-\nabla^2\rho$ maximum from the nucleus; DD_n^L $d^2(-\nabla^2\rho)/dr^2$ at r_n; ··· maximum does not appear.]

	n	r_n^L	$(-\nabla^2\rho)_n$	DD_n^L	r_{n-1}^L	$(-\nabla^2\rho)_{n-1}$	DD_{n-1}^L	
Be	2	1.592	0.0273	0.587				
Mg	3	2.548	0.0015	0.047	0.395	55.829	17420	
Ca	4	3.754	**−0.0001**	0.004	0.894	3.860	383	IIa
Sr	5	4.378	**−0.0003**	0.001	1.276	0.181	46	
Ba	6	5.165	**−0.0002**	0.0003	1.739	**−0.137**	4	
Cu	4	···	···	···	0.531	66.099	17812	
Ag	5	···	···	···	0.826	12.533	2099	Ib
Au	6	···	···	···	···	···	···	
Zn	4	···	···	···	0.505	86.830	25085	
Cd	5	···	···	···	0.792	16.843	3047	IIb
Hg	6	···	···	···	1.057	**−3.671**	117	
B	2	1.187	0.1412	5.395				
Al	3	2.078	0.0090	0.290	0.358	96.630	36500	
Ga	4	···	···	···	0.482	113.058	36569	IIIa
In	5	···	···	···	0.761	22.323	4307	
Tl	6	···	···	···	1.015	**−3.896**	257	
C	2	0.941	0.4957	29.864				
Si	3	1.754	0.0346	1.313	0.326	158.800	71567	
Ge	4	···	···	···	0.461	146.293	51562	IVa
Sn	5	···	···	···	0.732	29.178	5945	
Pb	6	···	···	···	0.971	**−4.107**	543	

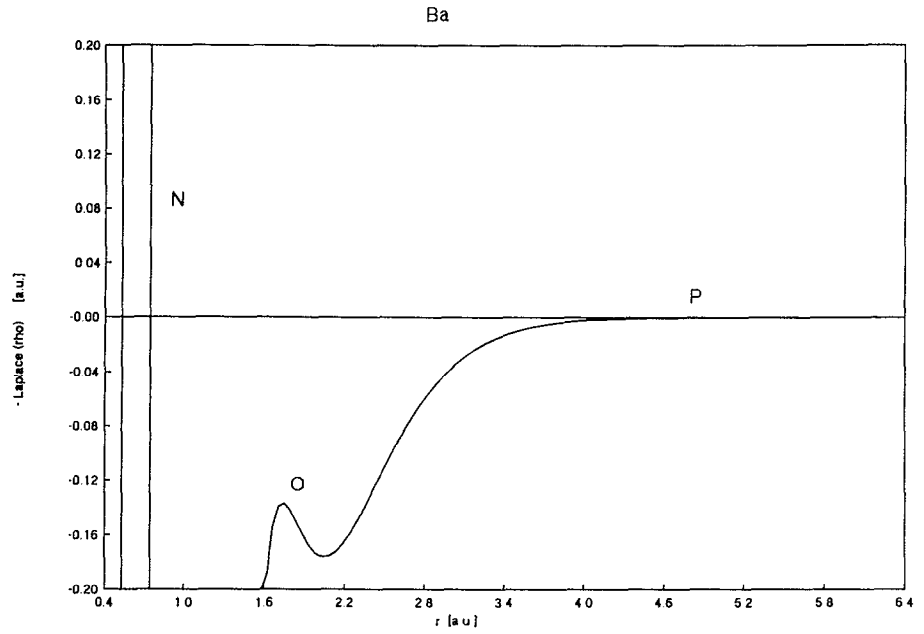

FIG. 1. $-\nabla^2\rho$ for the Dirac–Fock calculation of Ba. The shells are marked by capital letters.

guishable for the fifth row atoms Ag–Sn and the sixth row (!) atom Au. In the case of the alkaline-earth metals Ca–Ba, we find a valence maximum and minimum in the $-\nabla^2\rho$ diagrams, but both negative, cf. Table I. As seen from Fig. 1, for Ba (sixth row) this is true even for the penultimate shell. Hence, there is no valence charge concentration for these atoms. All these results are consistent with those of Boyd.[2] This shows that the relativistic densities bring no qualitative changes in the analysis of $-\nabla^2\rho$ in comparison to the nonrelativistic densities used by Sagar *et al.*[6] or Shi and Boyd.[7]

The missing $-\nabla^2\rho$ maximum for the valence shell of the heavy atoms is due to the influence of the *d* orbitals. The Laplacian of the total electron density ρ is equal to the sum of the orbital contributions $\nabla^2\rho_i$. For each orbital, the outermost $-\nabla^2\rho_i$ region is a negative one. In the valence region, the charge depletion of the *d* orbitals from the penultimate shell in the valence region is overwhelming the charge concentration of the valence *s* and *p* orbitals. This effect is even increased by the relativistic expansion of the *d* orbitals and the contraction of the *s* orbitals. Figure 2 shows $-\nabla^2\rho$ for Ga computed with the total density (a); the valence maximum is missing. If the 3*d*-orbital contribution $-\nabla^2\rho_d$ is substracted from the $-\nabla^2\rho$ for the total density, then the *N* shell appears (b). In addition, in the case of the atoms of the sixth row, we must account for the charge depletion of the *f* orbitals.

III. SHELL STRUCTURE WITH $-E_{\text{kin}}$

For the above mentioned atoms $-E_{\text{kin}}$ was derived from the numerically computed $\nabla^2\rho$ and $\nabla\rho$ following Eq. (4a). The number and sign of the minima in an $-E_{\text{kin}}$ vs *r* diagram was determined. At the nucleus, $-E_{\text{kin}}$ is negative infinite, as determined by the value of the Laplacian. This extremum will be designated as the first minimum. The behavior of $-E_{\text{kin}}$ at $r\to\infty$ can be easily found by inserting the expression for the electron density Eq. (5) in Eq. (4a). As $r\to\infty$, the $-E_{\text{kin}}$ approaches the value for the ionization potential of the system.[8,9,14]

According to Hunter's interpretation[8] of the negative and positive $-E_{\text{kin}}$ regions (classically allowed or forbidden, respectively), one should expect each shell to be characterized by a region of negative $-E_{\text{kin}}$. They should be separated by a region of positive $-E_{\text{kin}}$.

One can try to choose point descriptors to characterize shells. We suggest to use the extrema of $-E_{\text{kin}}$. The minima in $-E_{\text{kin}}$ would mark the shells, and the maxima the intershell regions. Please note that this does not exactly follow Hunter's proposal. In Hunter's proposal, the sign of $-E_{\text{kin}}$ changes when going from a shell to an intershell region. This must not hold for all atoms if using the extrema as the shell descriptors (see Fig. 14). Another attempt to define point descriptors to characterize shells was given by Sagar *et al.*[9] They choose the odd zeros of $-E_{\text{kin}}$ to define the shells and the even zeros for the intershell regions.

For each studied atom, the number of the $-E_{\text{kin}}$ minima corresponds with the position in the Periodic System of Elements so that an atom in the *n*th row exhibits *n* minima (Table II). So, as opposed to the Laplacian, in all cases, a descriptor for the valence shell was found. For the second row atoms Li–Ne, the first $-E_{\text{kin}}$ minimum (see above) describes the K shell, the maximum is ascribed to the KL

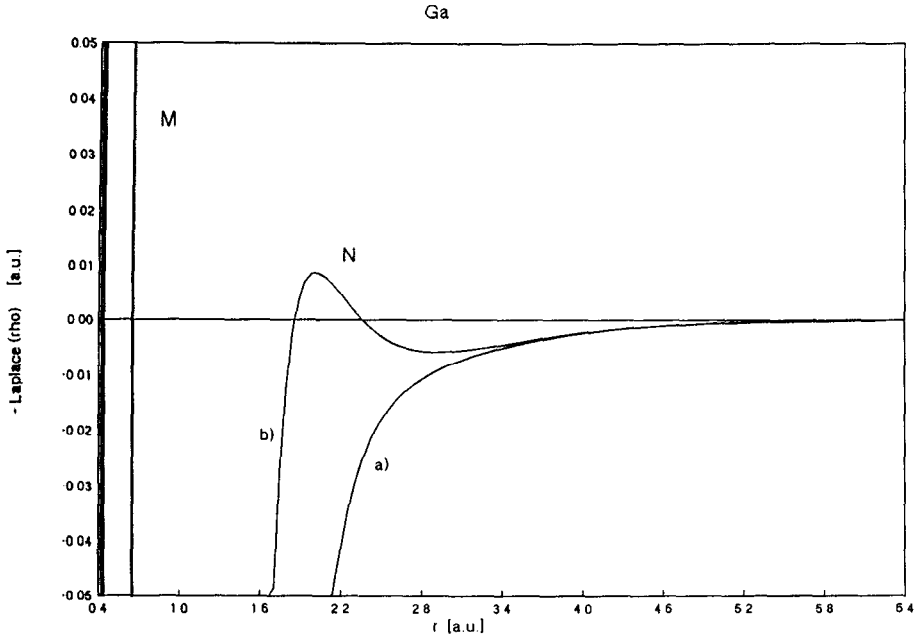

FIG. 2. $-\nabla^2\rho$ for the Dirac–Fock calculation of Ga; (a) diagram for the total density and (b) by omiting the 3d-orbital density. The shells are marked by capital letters.

intershell region, and the following minimum stands for the L shell, see Fig. 3 with $-E_{\rm kin}$ for the C atom. Figure 4 for Ba illustrates that for the atoms Be–Ba, the valence shell is located in a region of positive local kinetic energy (compare with $-\nabla^2\rho$, Sec. II). However, for the atoms Cu–Au, Zn–Hg, Ga–Tl, and Sn–Pb, the local $-E_{\rm kin}$ minimum indicating in our arbitrary assignment the valence shell is positioned in a region of positive $-E_{\rm kin}$.[9] As an example, see

TABLE II. $-E_{\rm kin}$ minima for the valence and the penultimate shell. The density was derived from a relativistic Dirac–Fock calculation (Ref. 17). All data are in atomic units. [n the principal quantum number of the valence shell; $-E_n^{\rm kin}$ nth $-E_{\rm kin}$ minimum; r_n^E the distance of the nth $-E_{\rm kin}$ minimum from the nucleus; $DD_n^E d^2(-E_{\rm kin})/dr^2$ at r_n.]

Element	n	r_n^E	$-E_n^{\rm kin}$	DD_n^E	r_{n-1}^E	$-E_{n-1}^{\rm kin}$	DD_{n-1}^E	
Be	2	1.665	−0.372	3.347				
Mg	3	2.638	−0.137	0.758	0.419	−4.197	413	
Ca	4	3.822	−0.062	0.231	0.935	−1.645	64	IIa
Sr	5	4.360	−0.041	0.146	1.316	−0.639	19	
Ba	6	5.016	−0.028	0.092	1.731	−0.269	7	
Cu	4	4.419	**0.065**	0.039	0.556	−3.701	375	
Ag	5	5.301	**0.083**	0.026	0.857	−1.998	132	Ib
Au	6	5.521	**0.163**	0.011	1.054	−0.447	37	
Zn	4	3.255	**0.043**	0.138	0.530	−4.078	440	
Cd	5	4.064	**0.077**	0.065	0.823	−2.243	156	IIb
Hg	6	4.331	**0.156**	0.028	1.019	−0.527	47	
B	2	1.245	−0.600	9.154				
Al	3	2.156	−0.215	1.814	0.380	−5.206	602	
Ga	4	2.733	**0.013**	0.321	0.507	−4.493	529	IIIa
In	5	3.525	**0.056**	0.106	0.791	−2.511	191	
Tl	6	5.408	**0.114**	0.002	0.991	−0.635	58	
C	2	0.989	−0.875	20.095				
Si	3	1.823	−0.322	3.766	0.347	−6.336	863	
Ge	4	2.339	−0.033	0.793	0.485	−4.954	626	IVa
Sn	5	3.038	**0.034**	0.242	0.761	−2.800	229	
Pb	6	3.500	**0.102**	0.066	0.96	−0.740	65	

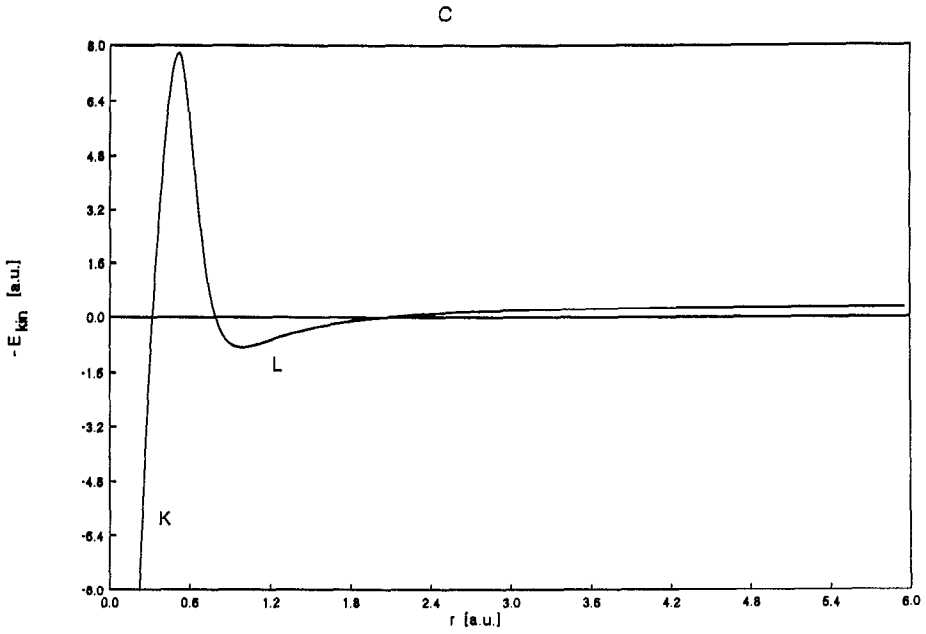

FIG. 3. $-E_{\text{kin}}$ for the Dirac–Fock calculation of the C atom. The shells are marked by capital letters.

Fig. 10 (in the valence region, the $-E_{\text{kin}}$ for the 22 electron pseudopotential calculation is identical with the all electron $-E_{\text{kin}}$). In such a region, the electron is classically not allowed. The value of the valence $-E_{\text{kin}}$ minimum, as well as the shallowness of the curve in this region, increases down the column. (For the curvature of the $-E_{\text{kin}}$ vs r curve at the nth $-E_{\text{kin}}$ minimum, see the parameter DD_n^E in Table II). On the other hand, in each of the row series Cu–Ge, Ag–Sn, and Au–Pb, the valence $-E_{\text{kin}}$ minimum becomes deeper and more pronounced with increasing atomic number. The result of this trend, see Table II, is a valence shell with positive local kinetic energy for Ge.

The spurious oscillations in $-E_{\text{kin}}$ found by Sagar *et al.*[9] in the valence region of some atoms did not appear in our

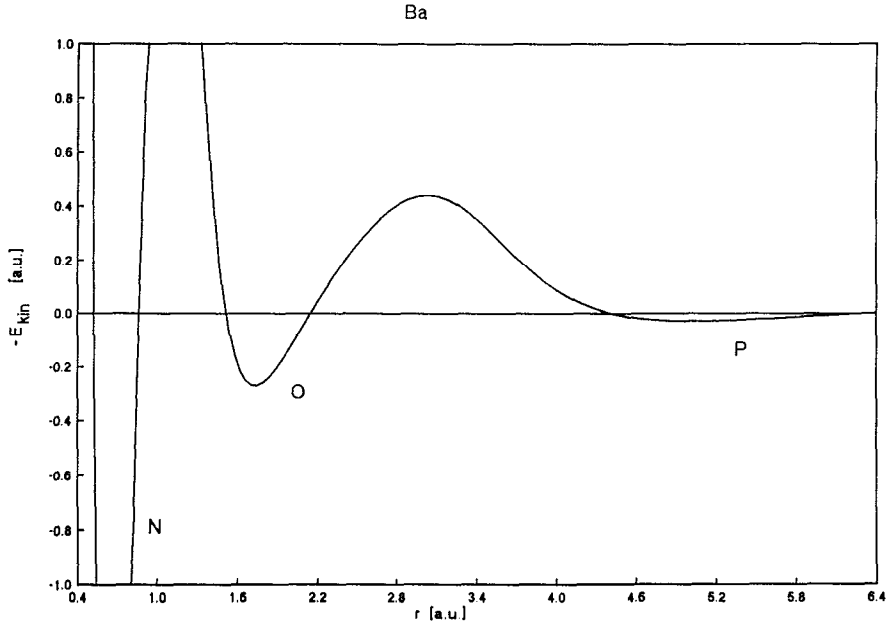

FIG. 4. $-E_{\text{kin}}$ for the Dirac–Fock calculation of Ba. The shells are marked by capital letters.

numerical (relativistic and nonrelativistic) calculations. We thus believe that this indicates a sensitivity of the shape of $-E_{\rm kin}$ to basis sets—especially at large distances [Sagar *et al.* used nonrelativistic self-consistent-field (SCF) wave functions of Clementi and Roetti[18] and McLean and McLean[19]].

The factor $1/\rho$ in the expression for $-E_{\rm kin}$, Eq. (4), makes it impossible to split $-E_{\rm kin}$ into the orbital contributions. Nevertheless, the orbitals with the same principal quantum number exhibit their main contribution to the total density at nearly the same distance from the nucleus. Thus, orbitals within a particular shell are predominant in the sum of the orbital densities $\Sigma\rho_i$. If we neglect the contributions from the remaining shells, then we can analyze $-E_{\rm kin}$ into the shell contributions and assign each well in $-E_{\rm kin}$ to a particular shell. In the fourth row, the occupied valence orbitals are the $4s$ and, if required, $4p$. The occupied orbitals in the preceding shell are the $3s$ and $3p$ in the case of Ca, but $3s$, $3p$, and $3d$ for the successive elements. The effect is a worse separability of the two outermost shells. The separability is improved with increasing atomic number as confirmed by the trend of $-E_{\rm kin}$ described above. The $3d$ density has also an influence on the $-E_{\rm kin}$ value in the valence region. More specifically, in the Laplacian part of Eq. (4) the charge depletion coming from the d orbitals neglects the charge concentration in the valence shell. The result of this influence is a negative local kinetic energy in the valence region.

IV. SHELL STRUCTURE AS DESCRIBED BY $-|\nabla\rho|/\rho$

For the investigated atoms, $-|\nabla\rho|/\rho$ was computed utilizing the numerically derived $\nabla\rho$ (cf. Sec. I). The $1/\rho$ factor prevents the separation of $-|\nabla\rho|/\rho$ into orbital contributions. With the same arguments as in the case of $-E_{\rm kin}$, it is possible to split the expression for the total density $-|\nabla\rho|/\rho$ in individual shell terms where s is a shell index. If the expression

$$-|\nabla\rho|/\rho = \sum\left(-|\nabla\rho_s|\sum\rho_s\right)\rightarrow -|\nabla\rho_s|/\rho_s \qquad (7)$$

for each shell is applicable and the shell electron density ρ_s is described by Eq. (5) with different λ_s for each shell, then we obtain a step-like $-|\nabla\rho|/\rho$ diagram.

Suppose the total density can be divided into shell densities ρ_s that are undisturbed by the remaining shell densities and given by Eq. (5) with $\varkappa = 0$. This is in accordance with the model of piecewise exponentially decay of the electron density as proposed by Wang and Parr.[16] A $-|\nabla\rho|/\rho$ diagram then consists of plateaus, each corresponding to a particular shell, of constant $-|\nabla\rho|/\rho$ values. The steps in such a diagram are rectangular. In general, for an arbitrary $\varkappa$,

$$-|\nabla\rho|/\rho = -2|(\varkappa/r-\lambda)|, \qquad (8)$$

and the $-|\nabla\rho|/\rho$ in each shell is now r dependent. The constancy of $-|\nabla\rho|/\rho$ is largely valid for the valence plateau. The plateaus for the inner shells are shorter and strongly curved as moving toward the nucleus (Fig. 5). The rectangular steps between the plateaus hold only for the simplified picture of undisturbed shell densities. But, for an atomic calculation, there is a mutual penetration of the shell densities ρ_s in the shell boundary region. This will decrease the slope of the shell density at the boundary to the next shell, and the change to the following shell occurs not immediately, but takes place within certain distance. The higher

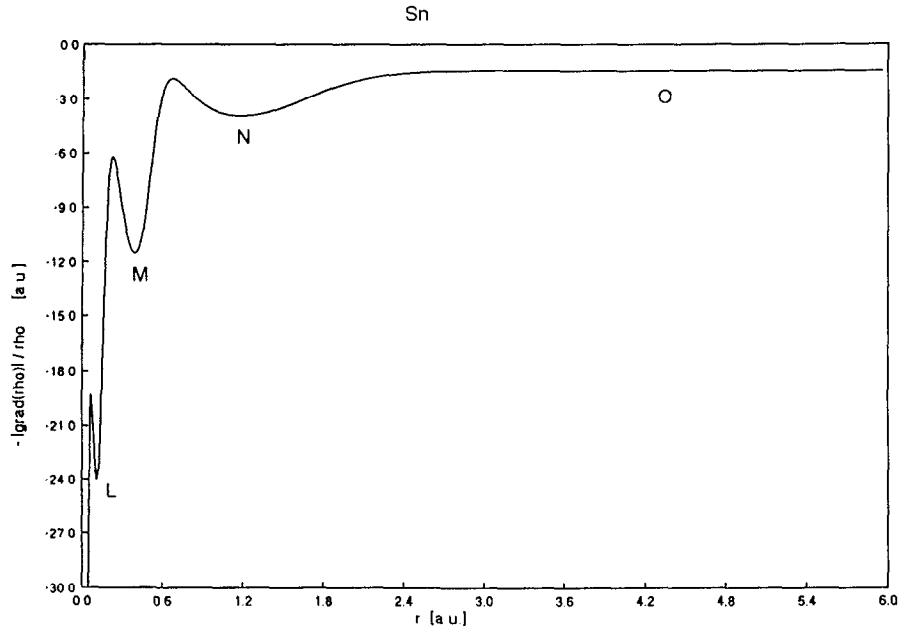

FIG. 5. $-|\nabla\rho|/\rho$ for the Dirac–Fock calculation of the Sn atom. The shells are marked by capital letters.

TABLE III. The $-|\nabla\rho|/\rho$ values calculated from the first ionization potential, and the data for the valence shell obtained from the diagrams for the relativistic Dirac–Fock calculations (Ref. 17). All data are in atomic units. [-IP (I.) the first ionization potential (Ref. 30) in a.u.; $\varkappa$, -2λ see Eqs. (5) and (8); $(-|\nabla\rho|/\rho)_{\text{Korr6}}$ the $-|\nabla\rho|/\rho$ value calculated at 6 a.u. from the nucleus; following Eqs. (5) and (8) and using the IP (Ref. 30); $(-|\nabla\rho|/\rho)_6$ the $-|\nabla\rho|/\rho$ value at 6 a.u. from the nucleus; $(-|\nabla\rho|/\rho)_{\text{Barr}}$ the $-|\nabla\rho|/\rho$ value for the valence barrier; r_{Barr} the distance of the barrier from the nucleus; ··· barrier does not appear.]

	$-$IP (I.)	$\varkappa$	-2λ	$(-\lvert\nabla\rho\rvert/\rho)_{\text{Korr6}}$	$(-\lvert\nabla\rho\rvert/\rho)_6$	$(-\lvert\nabla\rho\rvert/\rho)_{\text{Barr}}$	r_{Barr}	
Be	0.343	0.21	−1.66	−1.59	−1.47	−0.52	1.42	
Mg	0.281	0.33	−1.50	−1.39	−1.26	−0.82	2.37	
Ca	0.225	0.49	−1.34	−1.18	−1.00	−0.73	3.47	IIa
Sr	0.209	0.55	−1.29	−1.11	−0.91	−0.73	3.98	
Ba	0.191	0.62	−1.24	−1.03	−0.79	−0.69	4.60	
Cu	0.284	0.33	−1.51	−1.40	−1.25	−1.24	5.13	
Ag	0.278	0.34	−1.49	−1.38	−1.23	···	···	Ib
Au	0.339	0.21	−1.65	−1.58	−1.50	···	···	
Zn	0.345	0.20	−1.66	−1.60	−1.43	−1.39	3.66	
Cd	0.330	0.23	−1.62	−1.55	−1.38	−1.36	4.65	IIb
Hg	0.383	0.14	−1.75	−1.70	−1.56	···	···	
B	0.305	0.28	−1.56	−1.47	−1.66	−0.81	1.06	
Al	0.220	0.51	−1.33	−1.16	−1.28	−0.89	1.93	
Ga	0.220	0.51	−1.33	−1.16	−1.27	···	···	IIIa
In	0.213	0.53	−1.31	−1.13	−1.25	···	···	
Tl	0.224	0.50	−1.34	−1.17	−1.30	···	···	
C	0.414	0.10	−1.82	−1.79	−1.95	−1.14	0.85	
Si	0.299	0.29	−1.55	−1.45	−1.53	−0.92	1.62	
Ge	0.290	0.31	−1.52	−1.42	−1.50	−1.47	2.33	IVa
Sn	0.270	0.36	−1.47	−1.35	−1.44	−1.40	3.12	
Pb	0.273	0.32	−1.48	−1.37	−1.43	···	···	

the mutual penetration, the longer the distance. The averaged shell densities exhibit some maxima along the r axis;[1] the outermost one mainly determines the density in the particular shell region. If the density ρ_s at the shell boundary decreases significantly before the density of the next shell can reach its maximum, the slope of the total density also decreases in the boundary region. There we then find a λ value, see Eq. (5), less then the values for the two adjacent shells. The stronger such a separation of the shell densities, the smaller the boundary λ value will be. Thus, the $-|\nabla\rho|/\rho$ diagram of an atom, e.g., Sn in Fig. 5, exhibit plateaus (possibly curved) one for each shell, separated by barrier like walls and linked (for large r) to IP via Eq. (5). For the inner shells, the width of a plateau is comparable to that of the adjacent barriers.

In Table III are summarized the valence shell data for the Dirac–Fock calculations. Essential for the representation of a shell is a plateau. A barrier is not necessary in any case, as exhibited by Ag, Au, Hg, and Ga, In, Tl (and in outlines by Sn, Fig. 5). It merely indicates the poor separation of the valence and the penultimate shell. Moreover, comparing the position of a valence barrier with that of the $-\nabla^2\rho$ or E_{kin} maximum (Tables I–III and Fig. 6) leads to the conjecture that the barrier is a part of the valence shell. The $-|\nabla\rho|/\rho$ values calculated from the first IP, Eqs. (5) and (8), are also set out in Table III. At a distance of 6 a.u. from the nucleus, these theoretical values for the valence plateau are about 10% higher than those for the Dirac–Fock calculations, for elements with occupied p orbitals. It is just the reverse in the case of elements with unoccupied p orbitals.

V. TEST OF BASIS SET QUALITY WITH $-|\nabla\rho|/\rho$

The linear combinations of Gaussian functions, $\Sigma c_k \exp(-\alpha_k r^2)$, are widely used as the basis sets in the Hartree–Fock (HF) calculations. The density gradient then obeys the function $r\Sigma\alpha_k c_k \exp(-\alpha_k r^2)$, where r is the distance from nucleus. For large distances, the term with the smallest exponent dominates in the sum of Gaussian functions and the linear decay sets on, i.e., $-|\nabla\rho|/\rho$ behaves like a linear function of r. In addition, at the position of the nucleus $-|\nabla\rho|/\rho = 0$. Thus, a $-|\nabla\rho|/\rho$ diagram for a Gaussian basis set displays additionally a peak at $r = 0$ and a linear decay to $-\infty$ for large r. To test the range of this behavior, we have computed $-|\nabla\rho|/\rho$ for the H atom with the STO–3G and STO–6G[20,21] basis sets. In Fig. 7, the peak at $r = 0$ in the diagram for the STO–3G basis set (a) is wide, followed by oscillations of the plateau that are strong compared to that for STO–6G (b). At approximately 4.5 a.u. from the nucleus, the linear decay sets on in case of STO–3G. (For the exact hydrogen density, $-|\nabla\rho|/\rho$ is equal to -2 at every distance.) This leads to the conclusion that a very narrow zero peak plateaus without oscillations, and a late onset of the linear decay indicate a basis set that satisfactorily models the exact electron density.

In order to investigate the influence of the basis sets on $-|\nabla\rho|/\rho$, we compared the diagrams for the numerical and

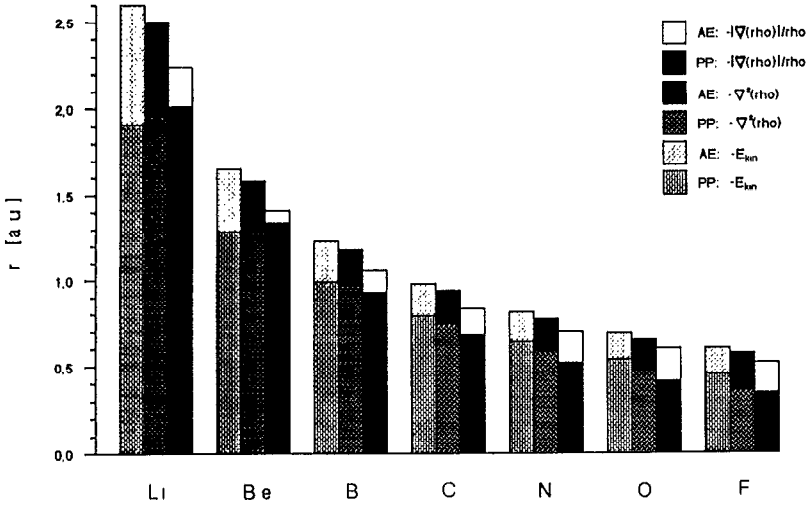

FIG. 6. All electron (AE) and pseudopotential (PP) calculations of Li–F. The distances of the $-\nabla^2\rho$ maxima, $-E_{kin}$ minima, and $-|\nabla\rho|/\rho$-barriers (nodes for PP) from the nucleus.

HF calculations for the atoms Li–F. In the HF calculations, an STO–3G[20,21] and the basis sets from Lie and Clementi[22] were used. All diagrams exhibit two plateaus as expected for the second row atoms. The results for the Lie/Clementi basis sets are in high accordance with the numerical ones. The zero peaks are almost not perceptible, as seen in Fig. 8 for nitrogen (a), and the linear decay is noticeable (considering the r range 0–6 a.u.) not till oxygene. For the STO–3G basis sets the zero peaks are rather broad and the first shell plateaus are disturbed by oscillations, cf. Fig. 8 for nitrogen (b). The valence plateaus are without oscillations, but the linear decay sets on at a distance of 4.5 (Be) to 2.5 (F) a.u. from the nucleus. With that, the STO–3G density is described somewhat properly in the valence region, starting at the boundary barrier and extending about 1–3 a.u. in the outer region. For a particular atom the distances of the boundary

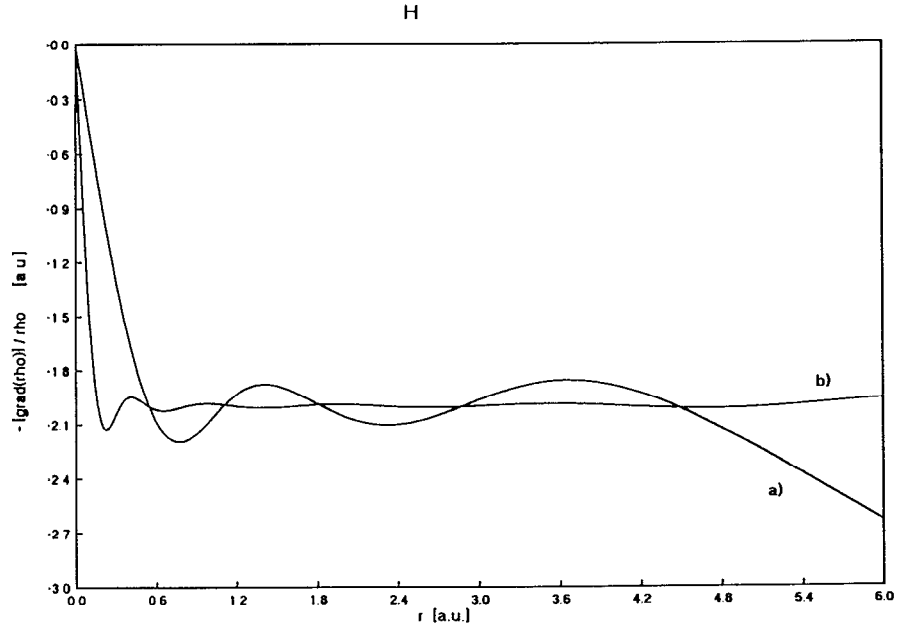

FIG. 7. $-|\nabla\rho|/\rho$ for the HF calculation of hydrogen with (a) the STO–3G and (b) the STO–6G basis set (Refs. 20 and 21).

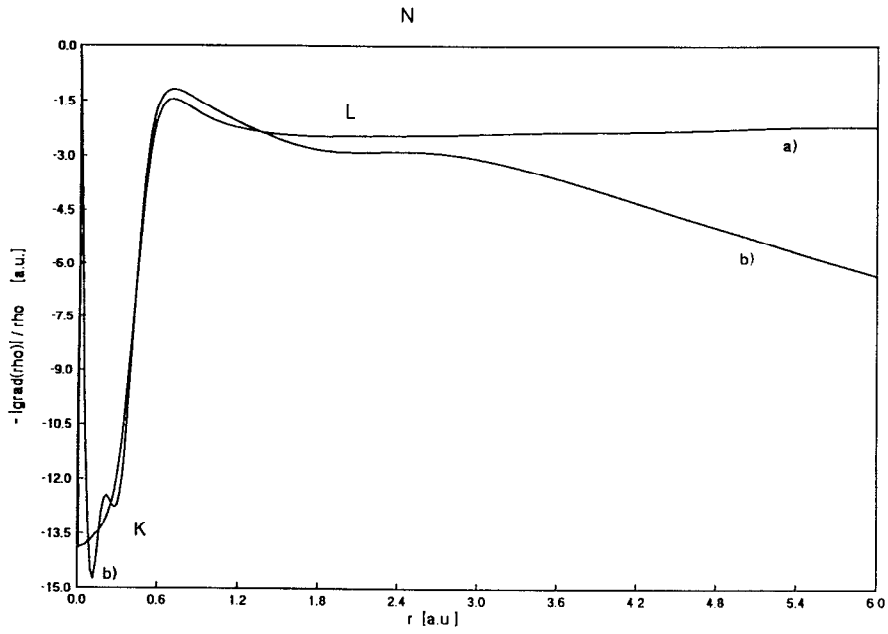

FIG. 8. $-|\nabla\rho|/\rho$ for the HF calculation of nitrogen. The all electron calculations were realized with (a) the Lie/Clementi (Ref. 22) and (b) the STO–3G (Refs. 20 and 21) basis set. The shells are marked by capital letters.

barriers from the nucleus are independent of the calculation method, although only the $-|\nabla\rho|/\rho$ barrier values for the Lie/Clementi basis are almost identical with the numerical ones.

VI. THE EFFECT OF RELATIVITY ON $-\nabla^2\rho$, $-|\nabla\rho|/\rho$, AND $-E_{\text{kin}}$

The effect of relativity on the energy and the orbital density distributions of atoms was intensively examined in the past.[23–25] Some important results of these investigations are the relativistic contraction of the s and p orbitals, the relativistic self-consistent expansion of the d and f orbitals, and the spin–orbit splitting of the orbitals with the angular momentum larger than zero.[23]

To examine the effect of relativity on $-\nabla^2\rho$, $-E_{\text{kin}}$, and $-|\nabla\rho|/\rho$, the relativistic and the nonrelativistic calculations of the IIIa group atoms B–In and the sixth row atoms Ba, Au, Hg, Tl, and Pb were compared. The nonrelativistic calculations were performed with the MCDF[17] program using the speed of light multiplyed by one thousand. The nonrelativistic results for B–In (Table IV) are almost the same as in the relativistic case. There are only small deviations, the largest, as expected, for In—the heaviest element in this series. But the qualitative picture did not change. For the (nonrelativistic) atoms, Ga and In, there are no valence maxima in $-\nabla^2\rho$, the valence minima in $-E_{\text{kin}}$ have a positive value, and there are no valence barriers in $-|\nabla\rho|/\rho$.

Let us now look at the sixth row atoms Ba, Au, Hg, Tl, and Pb (Table V). In the case of these heavy atoms, a significant effect of relativity should be expected. Indeed, we found some qualitative changes concerning $-\nabla^2\rho$ for the penultimate (O) shell. The nonrelativistic Au exhibits, in contrast to the relativistic result, a maximum for the O shell (although located in a region of charge depletion). For the nonrelativistic calculations of Hg, Tl, and Pb, the $-\nabla^2\rho$ maxima for the O shell have a positive $-\nabla^2\rho$ value. This indicates a region of charge concentration (remember that the corresponding relativistic $-\nabla^2\rho$ maxima are located in a region of charge depletion). The O shell maximum is made up mainly from the 5s, 5p, and 5d charge concentration reduced mainly by the 4s, 4p, 4d, and 4f charge depletion. In the case of the nonrelativistic calculations where the maximum is positive, the O shell charge concentration is overwhelming the N shell charge depletion. In the relativistic calculations, the s and p charge concentrations move toward the nucleus at the same time being higher and steeper. The effect on the d and f charge depletions is not so dramatic. These move a bit outward and become more shallow. The result is that the O shell charge concentration is now located in a region of higher charge depletion and the O shell $-\nabla^2\rho$ maximum is negative. The 5s and 5p orbital relativistic contraction is small for Ba and so is the change of the O shell $-\nabla^2\rho$ maximum. The contraction, as well as the shift of the O shell, $-\nabla^2\rho$ maximum is stronger when proceeding to the heavier atoms (Au–Pb). On the other hand, there are almost no changes in $-\nabla^2\rho$ for the valence shell due to the relativity. The valence maximum is still not available for Au–Pb and aside from a small shift, still negative for the Ba atom. The charge concentration for the valence orbitals is

TABLE IV. The data (compare Tables I–III) for the nonrelativistic Dirac–Fock calculations (Ref. 17) for the IIIa group atoms. All data are in atomic units. All symbols have the same meaning as in Tables I–III.

	B	Al	Ga	In	Tl
r_n^L	1.187	2.080	...	...	...
$(-\nabla^2\rho)_n$	0.1411	0.0091	...	...	...
DD_n^L	5.388	0.291	...	...	...
r_{n-1}^L		0.358	0.487	0.769	0.987
$(-\nabla^2\rho)_{n-1}$		95.986	108.356	22.972	0.896
DD_{n-1}^L		36 126	34 626	4173	747
r_n^E	1.246	2.158	2.728	3.460	3.864
$-E_n^{kin}$	−0.600	−0.216	**0.002**	**0.033**	**0.049**
DD_n^E	9.149	1.817	0.352	0.151	0.091
r_{n-1}^E		0.381	0.511	0.799	1.007
$-E_{n-1}^{kin}$		−5.192	−4.412	−2.562	−1.068
DD_{n-1}^E		600	509	190	66
r_{Barr}	1.06	1.93	...	...	...
$(-\lvert\nabla\rho\rvert/\rho)_{Barr}$	−0.81	−0.89	...	...	...
$(-\lvert\nabla\rho\rvert/\rho)_6$	−1.66	−1.28	−1.27	−1.23	−1.21

too small compared to the charge depletion in the same region. The shifts of the valence orbitals don't have a perceptible effect on the total value of $-\nabla^2\rho$ in the valence region.

The relativistic effect on the $-E_{kin}$ distribution for the sixth row atoms is not so dramatic. The nonrelativistic $-E_{kin}$ minima for the O shell are slightly shifted and somewhat deeper, but have the same sign as the corresponding relativistic $-E_{kin}$ values. With exception of Tl, this also holds for the valence shell. For Tl, the shift of the valence $-E_{kin}$ minimum is large (1.5 bohr). The detailed examination of the Laplacian and the gradient part of the Eq. (4) reveals that this considerable shift can be attributed to the $\nabla^2\rho/(4\rho)$ part of the equation. The nonrelativistic valence minimum for the $\nabla^2\rho/(4\rho)$ is located at 3.9 bohr from the nucleus. The relativity shifts this minimum about 4 bohr farther outwards. The substraction of the $(\nabla\rho)^2/(8\rho)^2$ part leads to the $-E_{kin}$ minimum at 5.4 bohr. The explanation for the large relativistic shift of the $\nabla^2\rho/(4\rho)$ minimum can be sought in the combined action of the relativistic contraction and the small value of the shell density.

The $-\lvert\nabla\rho\rvert/\rho$ is linked to the ionization potential via Eqs. (5) and (8). The inclusion of the relativity into the calculation of an atom decreases its ground state energy. This consequently also lowers the $-\lvert\nabla\rho\rvert/\rho$ valence plateau (i.e., it moves to a higher absolute value) for this atom. As described in Sec. IV, the mutual penetration of the shell den-

TABLE V. The data (compare Tables I–III) for the nonrelativistic Dirac–Fock calculations (Ref. 17) for some sixth row atoms. All data are in atomic units. All symbols have the same meaning as in Tables I–III.

	Ba	Au	Hg	Tl	Pb
r_n^L	5.106	...	...	...	...
$(-\nabla^2\rho)_n$	**−0.0001**	...	...	...	...
DD_n^L	0.0005	...	...	...	...
r_{n-1}^L	1.735	1.064	1.022	0.987	0.950
$(-\nabla^2\rho)_{n-1}$	**−0.066**	**−0.463**	0.128	0.896	1.937
DD_{n-1}^L	5	326	635	747	561
r_n^E	5.098	5.63	4.412	3.864	3.302
$-E_n^{kin}$	−0.034	**0.072**	**0.069**	**0.049**	**0.022**
DD_n^E	0.084	0.023	0.028	0.091	0.112
r_{n-1}^E	1.756	1.074	1.040	1.007	0.974
$-E_{n-1}^{kin}$	−0.327	−0.783	−0.918	−1.068	−1.228
DD_{n-1}^E	8	46	60	66	43
r_{Barr}	4.64	...	4.82	...	3.36
$(-\lvert\nabla\rho\rvert/\rho)_{Barr}$	−0.64	...	−1.29	...	−1.33
$(-\lvert\nabla\rho\rvert/\rho)_6$	−0.75	−1.17	−1.30	−1.21	−1.38

sities exercises an influence on the slope and the height of the barrier between the $-|\nabla\rho|/\rho$ plateaus for these shells. The relativistic orbital densities penetrate each other to a larger extent. The barrier between the penultimate and the valence shell is less developed and the change between the plateaus occurs during a longer distance for the relativistic calculations. Because the effect of relativity is strongly pronounced only for the heavy atoms, we also find the above described changes especially for the sixth row atoms. But relativity has no influence on the number of the $-|\nabla\rho|/\rho$ plateaus.

VII. THE INFLUENCE OF PSEUDOPOTENTIALS

The pseudopotentials are applied to reduce the costs of a molecular calculation. In such calculations, the effect of the core electrons is replaced by a pseudopotential. The missing core density give rise to a pseudopotential hole in the total density around the nucleus. With increasing distance from the nucleus, the density is growing to approach a maximum. After this maximum, the pseudopotential density closely follows the exponential descent of the all-electron density. To investigate the influence of pseudopotential on $-\nabla^2\rho$, E_{kin}, and $-|\nabla\rho|/\rho$, let us focus on the changes in the valence region.

The valence maxima of $-\nabla^2\rho$ for the pseudopotential calculations of Li–F (Lie/Clementi basis set;[22] pseudopotential parameters[26–28]) are 2–3 times higher and somewhat closer to the nucleus compared to the all-electron case (for Be cf. Fig. 9). This is due to the absent charge depletion of the $1s$ core density. As mentioned in Sec. II, starting with the fourth row, the Laplacian of the all-electron density is not able to represent the valence shell. Now let us look at the pseudopotential calculations of Sn. Using only four electrons[28] ($5s$, $5p$), the charge concentration for the valence shell appears (Fig. 10) due to the missing charge depletion of the fourth shell. But utilizing 22 electrons[29] ($4s$, $4p$, $4d$, $5s$, $5p$), the valence shell is again not available in $-\nabla^2\rho$.

The results for $-E_{\text{kin}}$ from the pseudopotential calculations of Li–F are similar to that for the Laplacian. The valence $-E_{\text{kin}}$ minima are closer to the nucleus and about two times larger in magnitude than in case of the all-electron density. Considering the all-electron calculations, the valence shell $-E_{\text{kin}}$ minimum was not negative (i.e., positive local kinetic energy) for some heavy atoms, see Sec. III. For a pseudopotential calculation of Sn with four electrons, the valence shell contains a region of positive local kinetic energy, but the $-E_{\text{kin}}$ minimum is located closer to the nucleus (corresponding to the position between the two outmost all-electron minima) and the E_{kin} value is too large (Fig. 11). As confirmed by Fig. 11, the 22 electrons pseudopotential calculation reproduces in the valence shell region, the all-electron result (Table II). However, now the $-E_{\text{kin}}$ minimum for the penultimate shell moves closer to the nucleus, whereby at the same time increasing its E_{kin} value. This seems to be a common feature for the shell immediately following the core.

For $-|\nabla\rho|/\rho$ evaluated with the pseudopotential density, a node is expected at the position of the density maximum. The numerical pseudopotential $-|\nabla\rho|/\rho$ diagrams exhibit two nodes, one in and the second (outer—the expect-

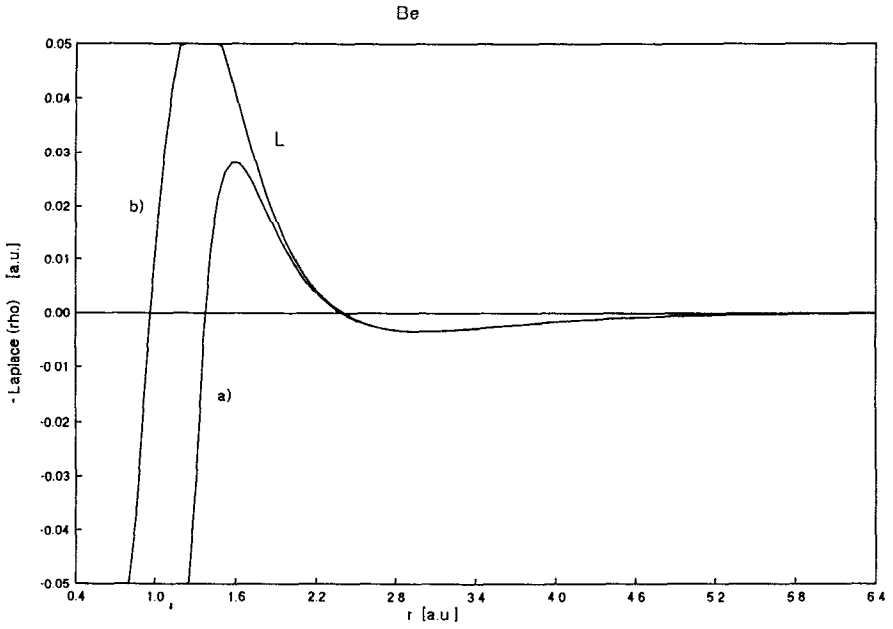

FIG. 9. $-\nabla^2\rho$ for the HF calculation of Be with the Lie/Clementi basis set (Ref. 22); (a) the all electron and (b) the pseudopotential calculation. The shells are marked by capital letters.

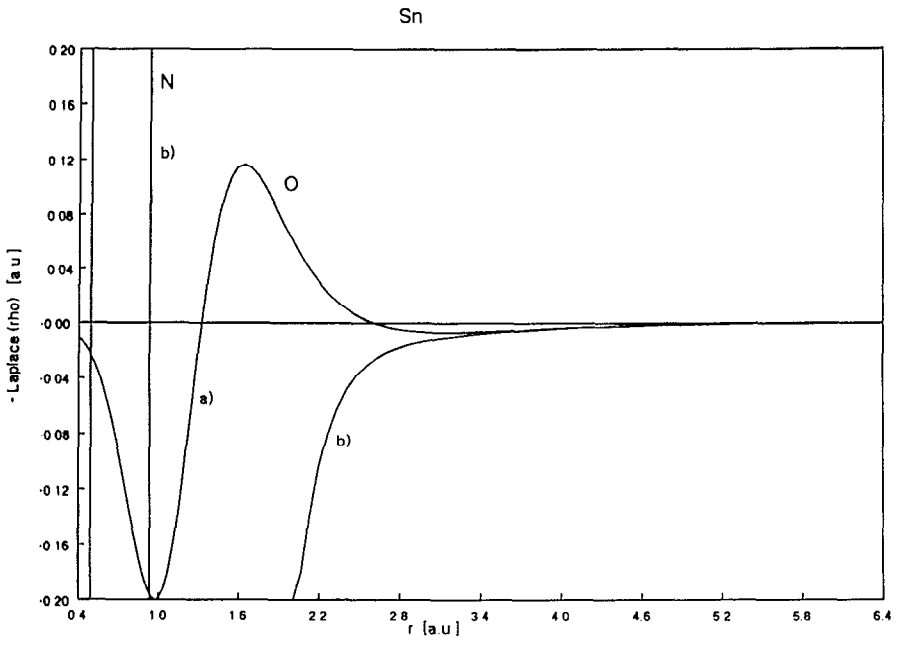

FIG. 10. $-\nabla^2\rho$ for the numerical pseudopotential calculation of Sn using (a) 4 and (b) 22 electrons. The shells are marked by capital letters.

ed one) at the boundary of the pseudopotential hole (cf. Fig. 12). The first node indicates a density minimum in the pseudopotential hole region due to the type of pseudopotential used in this paper. However, we are interested only in the valence density. Utilizing merely the last shell electrons in the pseudopotential calculations, the $-|\nabla\rho|/\rho$ diagram displays a node instead of the valence barrier. The node is positioned somewhat closer to the nucleus than the all-electron valence barrier (Fig. 13). Tracing the diagram further in the outer region, the curve is almost identical with the all elec-

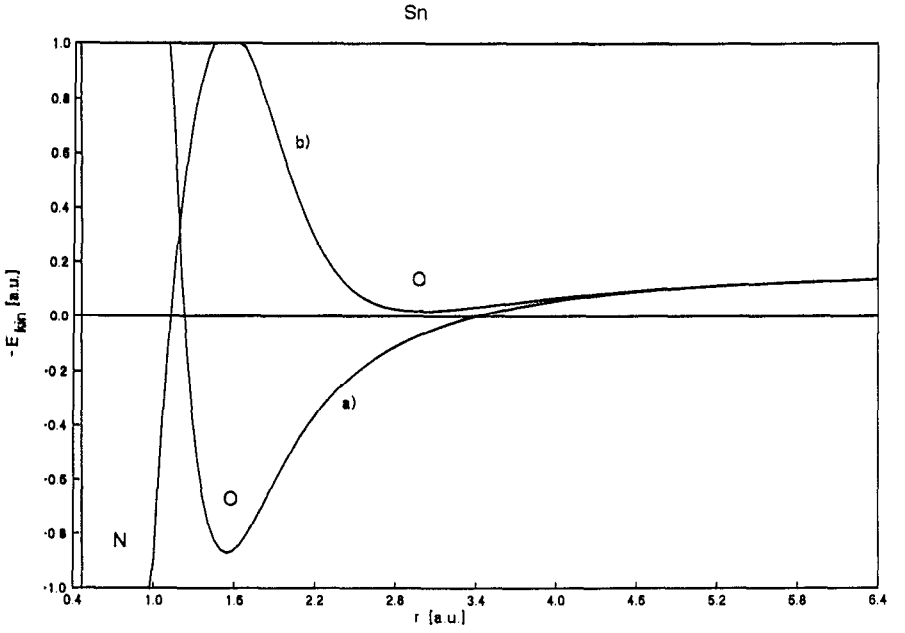

FIG. 11. $-E_{kin}$ for the numerical pseudopotential calculation of Sn using (a) 4 and (b) 22 electrons. The shells are marked by capital letters.

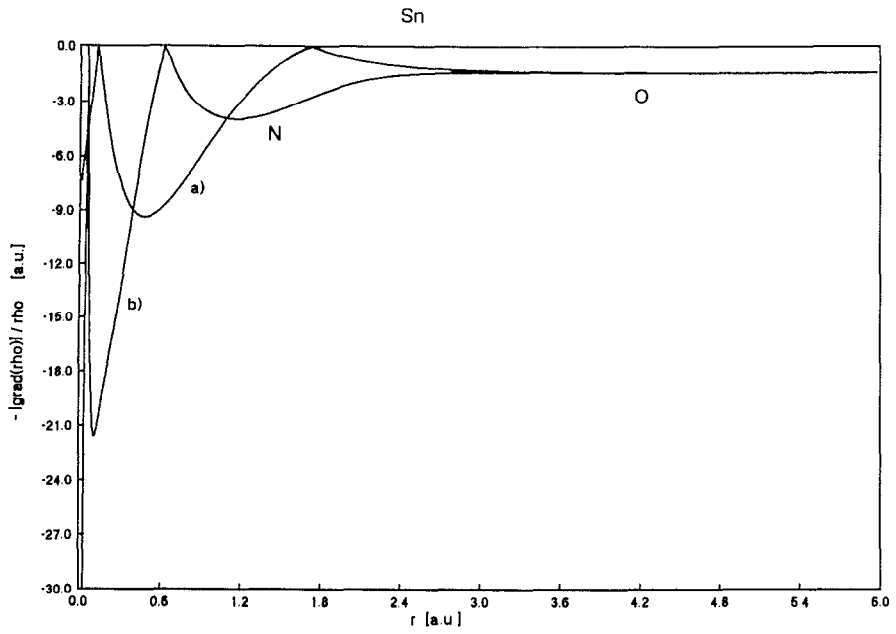

FIG. 12. $-|\nabla\rho|/\rho$ for the numerical pseudopotential calculation of Sn using (a) 4 and (b) 22 electrons. The shells are marked by capital letters.

tron result. This identity is approached at about 0.3 a.u. for the second row and a few a.u. for the heavy atoms after the node. In a diagram for a calculation with the electrons of the two last shells, cf. Fig. 12 for Sn, the outer node replaces the penultimate barrier. A short distance after the node, the plateaus for the two utilized shells and the boundary barrier are displayed. The positions of the plateaus are the same as in the all-electron curves.

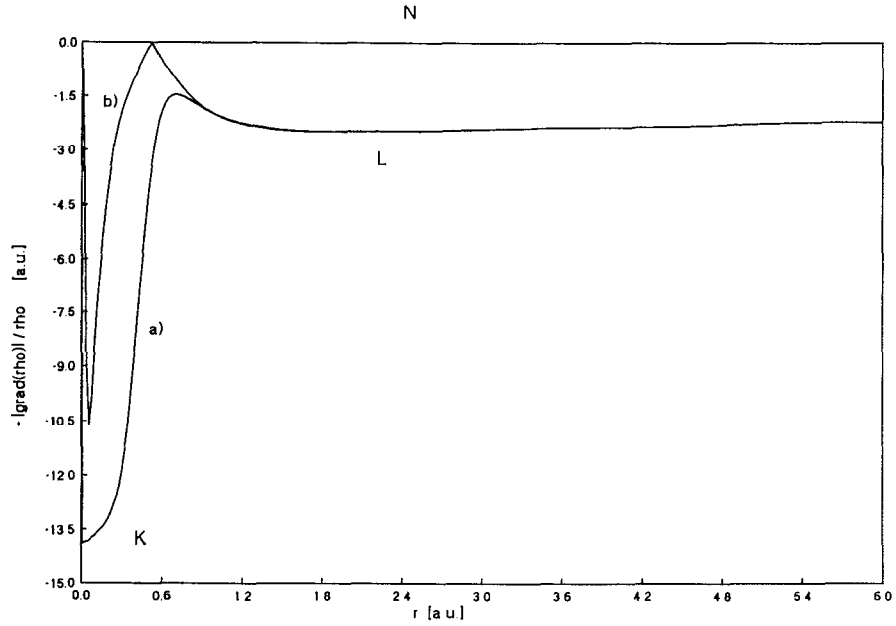

FIG. 13. $-|\nabla\rho|/\rho$ for the HF calculation of nitrogen. The all electron (a) and the pseudopotential (b) calculations were realized with the Lie/Clementi (Ref. 22) basis set. The shells are marked by capital letters.

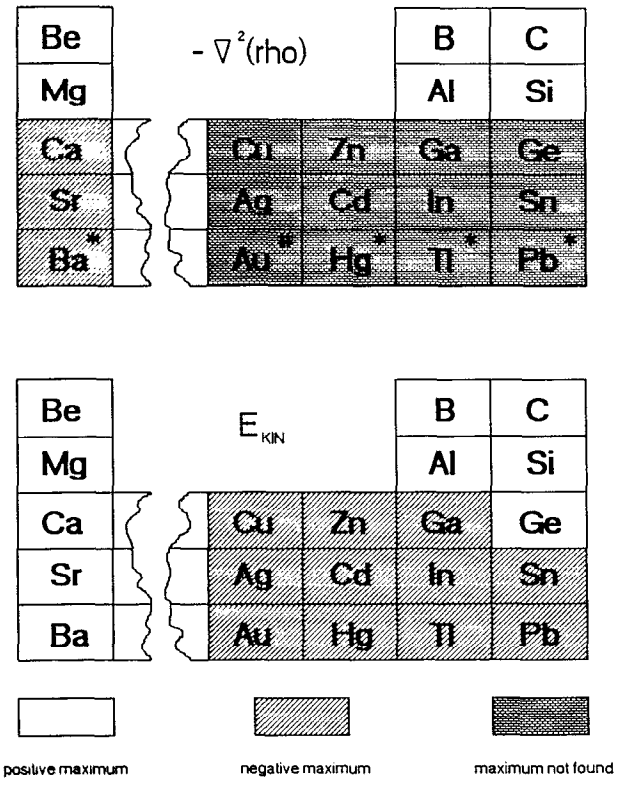

FIG. 14. Valence shell maxima in $-\nabla^2\rho$ and E_{kin} (i.e., $-E_{kin}$ minima) for some computed atoms. Data from relativistic Dirac–Fock calculations. # maximum for the valence and penultimate shell not found; * maximum for the penultimate shell is negative.

VIII. CONCLUSIONS

The presence of the valence shell in the diagrams of $-\nabla^2\rho$ and $-E_{kin}$ for part of the Periodic System of Elements is symbolically depicted in Fig. 14. The shell structure for the first to the third row atoms is correctly reproduced by means of all investigated quantities, i.e., $-\nabla^2\rho$, $-E_{kin}$, and $-|\nabla\rho|/\rho$. For any of these atoms, the valence $-\nabla^2\rho$ maxima and $-E_{kin}$ minima, together with the $-|\nabla\rho|/\rho$ valence barriers are located about the same distance from the nucleus. This holds for the all electron, as well as the pseudopotential calculations, for latter closer to the nucleus; see Fig. 6 for Li–F. The dependence of the $-\nabla^2\rho$ maxima position on the atomic number analyzed by Sagar *et al.*[6] and Shi and Boyd[7] can be applied also on E_{kin} and $-|\nabla\rho|/\rho$ (for the first two rows).

Another picture becomes evident for the atoms of the fourth and higher rows. Here, the Laplacian is not able to resolve the valence shell. Furthermore, the outermost minimum of $-E_{kin}$ describes the valence shell, but locates the latter in a region of negative local kinetic energy. Thus, only $-|\nabla\rho|/\rho$ indicates by means of the plateaus and barriers, the expected number of shells for every atom. The results for the pseudopotential calculations show that it is essential to use the two last shells to reproduce the all electron diagrams of $-\nabla^2\rho$, $-E_{kin}$, and $-|\nabla\rho|/\rho$. Using only the outermost shell causes an extremum ($-\nabla^2\rho$, $-E_{kin}$) or node ($-|\nabla\rho|/\rho$) to appear, again, all about the same range, but at approximately half the distance of the all-electron valence value (if available), as shown in Fig. 15. This can have a great effect on the interpretation of the respective diagrams

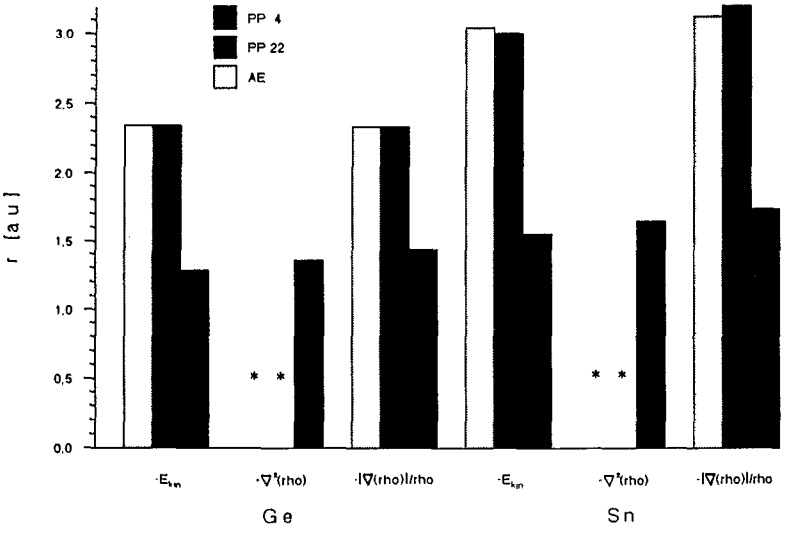

FIG. 15. All electron (AE) and pseudopotential (PP 4 and PP 22, i.e., with 4 and 22 electrons, respectively) calculations for Ge and Sn. The distances of the $-\nabla^2\rho$ maxima, $-E_{kin}$ minima, and $-|\nabla\rho|/\rho$ barriers (nodes for PP) from the nucleus. * maximum not available.

for the molecules. The analysis of the charge distribution of molecules will be the subject of another paper.

The consideration of the relativity in the atomic calculations yields some qualitative changes merely for the penultimate shell in the $-\nabla^2\rho$ representation of the heavy sixth row atoms. The effect on $-E_{\text{kin}}$ and $-|\nabla\rho|/\rho$ is, aside from some small shifts, negligible.

The quantity $-|\nabla\rho|/\rho$ can be used not only for the description of the shell structure, but also as a test for basis set quality.

ACKNOWLEDGMENT

The authors would like to thank Professor V. H. Smith, Jr., for his valuable comments and the encouraging discussion.

[1] J. T. Waber and D. T. Cromer, J. Chem. Phys. **42**, 4116 (1965).
[2] R. J. Boyd, Can. J. Phys. **56**, 780 (1978).
[3] A. M. Simas, R. P. Sagar, A. C. T. Ku, and V. H. Smith, Jr., Can. J. Chem. **66**, 1923 (1988).
[4] R. F. W. Bader, P. J. MacDougall, and C. D. H. Lau, J. Am. Chem. Soc. **106**, 1594 (1984).
[5] R. F. W. Bader and H. Essen, J. Chem. Phys. **80**, 1943 (1984).
[6] R. P. Sagar, A. C. T. Ku, V. H. Smith, Jr., and A. M. Simas, J. Chem. Phys. **88**, 4367 (1988).
[7] Z. Shi and R. J. Boyd, J. Chem. Phys. **88**, 4375 (1988).
[8] G. Hunter, Int. J. Quantum Chem. **29**, 197 (1986).
[9] R. P. Sagar, A. C. T. Ku, V. H. Smith, Jr., and A. M. Simas, Can. J. Chem. **66**, 1005 (1988).
[10] G. Sperber, Int. J. Quantum Chem. **5**, 189 (1971).
[11] G. Hunter, Int. J. Quantum Chem. **9**, 237 (1975).
[12] G. Hunter and C. C. Tai, Int. J. Quantum Chem. **19**, 1041 (1982).
[13] G. Hunter, *Density Matrices and Density Functionals*, edited by R. Erdahl and V. H. Smith, Jr. (Reidel, Dordrecht, 1987), pp. 583–596.
[14] M. Levy, J. P. Perdew, and V. Sahni, Phys. Rev. A **30**, 2745 (1984).
[15] M. Hoffman-Ostenhof and T. Hoffman-Ostenhof, Phys. Rev. A **16**, 1782 (1977).
[16] W.-P. Wang and R. G. Parr, Phys. Rev. A **16**, 891 (1977).
[17] I. P. Grant, B. J. McKenzie, P. H. Norrington, D. F. Mayers, and N. C. Pyper, Comput. Phys. Commun. **21**, 207 (1980).
[18] E. Clementi and C. Roetti, At. Data Nucl. Data Tables **14**, 177 (1974).
[19] A. D. McLean and R. S. McLean, At. Data Nucl. Data Tables **26**, 197 (1981).
[20] W. J. Hehre, R. F. Stewart, and J. A. Pople, J. Chem. Phys. **51**, 2657 (1969).
[21] E. Clementi and D. L. Raimondi, J. Chem. Phys. **38**, 2686 (1963).
[22] G. L. Lie and E. Clementi, J. Chem. Phys. **60**, 1275 (1974); F. B. van Duijneveldt, IBM Res. J. (#16437), 945 (1971).
[23] P. Pyykkö and J.-P. Desclaux, Acc. Chem. Res. **12**, 276 (1979).
[24] K. S. Pitzer, Acc. Chem. Res. **12**, 271 (1979).
[25] P. A. Christiansen, W. C. Ermler, and K. S. Pitzer, Ann. Rev. Phys. Chem. **36**, 407 (1985).
[26] P. Fuentealba, H. Preuss, H. Stoll, and L. v. Szentpaly, Chem. Phys. Lett. **89**, 418 (1982).
[27] P. Fuentealba, L. v. Szentpaly, H. Preuss, and H. Stoll, J. Phys. B **18**, 1287 (1985).
[28] G. Igel-Mann, H. Stoll, and H. Preuss, Mol. Phys. **65**, 1321 (1988).
[29] W. Plass, *Diplomarbeit* (Institut für Theoretische Chemie, Universität Stuttgart, 1987), p. 99.
[30] F. M. Page, *Handbook of Chemistry and Physics*, 58th ed., edited by R. C. Weast (CRC, Cleveland, Ohio, 1977), p. E–68.